



Minerva Access is the Institutional Repository of The University of Melbourne

Author/s:

Handcock, S;Richards, K;Karle, TJ;Kairath, P;Soch, A;Chavez, CA;Petrou, S;Maljevic, S

Title:

Three-Dimensional Morphological Characterisation of Human Cortical Organoids Using a Customised Image Analysis Workflow

Date:

2025-03-01

Citation:

Handcock, S., Richards, K., Karle, T. J., Kairath, P., Soch, A., Chavez, C. A., Petrou, S. & Maljevic, S. (2025). Three-Dimensional Morphological Characterisation of Human Cortical Organoids Using a Customised Image Analysis Workflow. *Organoids*, 4 (1), pp.1-1. <https://doi.org/10.3390/organoids4010001>.

Persistent Link:

<https://hdl.handle.net/11343/363269>

License:

[CC-BY](#)

## Article

# Three-Dimensional Morphological Characterisation of Human Cortical Organoids Using a Customised Image Analysis Workflow

Sarah Handcock <sup>1,†</sup> , Kay Richards <sup>1,†</sup> , Timothy J. Karle <sup>1</sup> , Pamela Kairath <sup>1</sup>, Alita Soch <sup>1</sup>, Carolina A. Chavez <sup>1</sup> , Steven Petrou <sup>1,2,3,\*</sup>  and Snezana Maljevic <sup>1,\*</sup> 

- <sup>1</sup> The Florey Institute of Neuroscience and Mental Health, University of Melbourne, Parkville, VIC 3052, Australia; sarah.handcock@florey.edu.au (S.H.); kay.richards@florey.edu.au (K.R.); timothy.karle@florey.edu.au (T.J.K.); alita.soch@florey.edu.au (A.S.); carolina.chavez@florey.edu.au (C.A.C.)  
<sup>2</sup> Praxis Precision Medicines, Inc., Cambridge, MA 02142, USA  
<sup>3</sup> Department of the Florey Institute, University of Melbourne, Parkville, VIC 3050, Australia  
\* Correspondence: steve.petrou@florey.edu.au (S.P.); snezana.maljevic@florey.edu.au (S.M.)  
† These authors contributed equally to this work.  
‡ Senior authors.

**Abstract: Summary Statement:** A tailored image analysis workflow was applied to quantify cortical organoid health, development, morphology and cellular composition over time. The assessment of cellular composition and viability of stem cell-derived organoid models is a complex but essential approach to understanding the mechanisms of human development and disease. **Aim:** Our study was motivated by the need for an image-analysis workflow, including high-cell content, high-throughput methods, to measure the architectural features of developing organoids. We assessed stem cell-derived cortical organoids at 4 and 6 months post-induction using immunohistochemistry-labelled sections as the analysis testbed. The workflow leveraged fluorescence imaging tailored to classify cells as viable and dying or non-viable and assign neuronal and astrocytic perinuclear markers to count cells. **Results/Outcomes:** Image acquisition was accelerated by capturing the organoid slice in 3D using widefield-fluorescence microscopy. This method used computational clearing to resolve nuclear and perinuclear markers and retain their spatial information within the organoid's heterogeneous structure. The customised workflow analysed over 1.5 million cells using DAPI-stained nuclei, filtering and quantifying viable and non-viable cells and the necrotic-core regions. Temporal analyses of neuronal cell number derived from perinuclear labelling were consistent with organoid maturation from 4 to 6 months of in vitro differentiation. **Overall:** We have provided a comprehensive and enhanced image analysis workflow for organoid structural evaluation, creating the ability to gather cellular-level statistics in control and disease models.

**Keywords:** brainoids; developmental disorders; genetic disease; image analysis



Academic Editor: Guillermo A Gomez

Received: 12 November 2024

Revised: 31 December 2024

Accepted: 13 January 2025

Published: 17 January 2025

**Citation:** Handcock, S.; Richards, K.; Karle, T.J.; Kairath, P.; Soch, A.; Chavez, C.A.; Petrou, S.; Maljevic, S. Three-Dimensional Morphological Characterisation of Human Cortical Organoids Using a Customised Image Analysis Workflow. *Organoids* **2025**, *4*, 1. <https://doi.org/10.3390/organoids4010001>

**Copyright:** © 2025 by the authors. Licensee MDPI, Basel, Switzerland. This article is an open access article distributed under the terms and conditions of the Creative Commons Attribution (CC BY) license (<https://creativecommons.org/licenses/by/4.0/>).

## 1. Introduction

The advent of stem cell research and the generation of organoid models using human embryonic stem cells (hESC) or, in particular, human-induced pluripotent stem cells (hiP-SCs) has seen personalised models of neurodevelopmental disorders made possible for the first time [1,2]

These human-derived stem cells multiply continuously in monolayer cultures while retaining the ability to differentiate into nearly any human cell type [1,2] The hiPSCs

originate as mature somatic cells, commonly fibroblasts obtained from skin samples, and are converted into pluripotent stem cells using reprogramming factors [1–3]. Several different approaches are available for differentiation into monolayer cultures, including dual-SMAD inhibition or the overexpression of transcription factors such as Neurogenin-2 [4]. Similarly, specific differentiation protocols are used for the generation of 3D organoid models, enabling the creation of more complex structures.

Three-dimensional (3D) brain or cerebral organoids have emerged as a groundbreaking technology with the potential to combine traditional laboratory findings with personalised clinical treatments [5,6]. These self-organising 3D structures closely mirror the neuronal organisation and functional activity of the developing human brain [2,5,6]. Depending on the protocol applied, they may represent cells from all brain regions, like cerebral organoids or the patterning of specific regions, such as the cortex, yielding so-called corticoids. The ability to produce cortical-specific organoids is crucial for investigating disease mechanisms of severe developmental disorders like developmental and epileptic encephalopathies (DEE) [7,8], autism spectrum [9,10] and Angelman syndrome [11]. In addition to the pathophysiology of neurodevelopmental disorders, these models can be used for therapeutic screening in a tissue-relevant context.

Despite the promise of organoid technology, small changes made by individual laboratories when implementing differentiation protocols contribute to structural heterogeneity in organoid models. Previous efforts to standardise organoid differentiation have aimed to reduce variability [12], but any adopted protocol still requires minor adjustments based on specific cell lines and procedures. Notably, the size, shape and viability of cortical organoids can vary significantly both within and between batches. To address this heterogeneity, we sought to create an image analysis workflow specifically designed to examine large datasets and benchmark the selected protocol. This imaging workflow would serve as an important exercise for the individual lab to achieve a level of standardisation. Specifically, it is to be applied to existing or newly adopted differentiation protocols to assure the consistency of data across experiments.

Evidence of cellular diversity in organoid models has primarily been drawn from measures of cell function, gene expression and protein abundance; however, these give little insight into architectural patterns of cell growth [13,14]. Recently, many groups have focused on high-throughput imaging methods to assess organoid morphology [15–18], and 3D spatial single cell and proteomic-based analysis methods have also emerged [19]. However, at the cellular level, high-resolution imaging techniques are still needed to measure the integrity of maturing organoids, which is challenging when applied to cortical organoids [13,14]. Additionally, the need for large sample datasets to obtain statistically valid comparisons creates a bottleneck in the imaging process. The ability to classify and count many cells via an automated system offers a promising solution to accelerate tissue analysis. Automating this process is especially important, as these models become more structurally complex as they mature. Current methods for evaluating organoids' intricate morphology using microscopy images include a variety of open source and commercially available tools (e.g., Fiji/Image J, CellProfiler and Imaris). These tools often require extensive tailoring to specific requirements.

Brain organoid maturation facilitates synaptic and network development, necessitating extended culturing periods, which ultimately results in larger tissue sizes [20,21]. Investigating the cellular architecture of these larger tissues often involves sectioning tissue and employing immuno-histochemistry (IHC), a widely used procedure for organoid analysis [14]. Other methods, such as tissue clearing, two-photon imaging, and light-sheet imaging, require specialised expertise and imaging systems, making them less commonly

used [14,19,22]. Our objective, therefore, was to develop a workflow using tissue sections as a more widely applicable image analysis method that could benefit various research groups.

One major challenge associated with large avascular organoids is their susceptibility to developing a necrotic core. A comprehensive structural analysis method must include a measurement approach that filters out dying cells and the necrotic core region [23]. The absence of a vascular system limits the diffusion of oxygen and nutrients from the surface of organoids, leading to the formation of a dead cell core as the organoids grow [24,25]. Despite the emergence of methods to improve nutrient diffusion, physical constraints limit nutrient flow to approximately 400  $\mu\text{m}$ , and in long-term 3D organoid cultures, hypoxic core susceptibility remains an issue [26–28]. Changes in the volume of dead cell cores or the percentage of dead cells may also reflect features of the disease model [4,29,30]. Image-based analyses have traditionally relied on the manual delineation of non-viable tissue boundaries, a process that is subjective, time-consuming and impractical for large sample sizes.

Another critical measurement we sought to address was obtaining cell counts for proteins expressed outside the nucleus or in peri-nucleic regions. While robust co-localisation imaging methods with cell nuclei are available, antibody labelling without spatial overlap—labelling non-nuclear proteins—presents a significant analytical challenge. Assigning these non-nuclear structures to a specific cell is non-trivial, as illustrated by antibodies marking filamentous structures. For example, microtubule-associated protein (MAP-2) is expressed in neuronal perikarya and dendrites, which, in cerebral organoids, have complex boundaries and lack stereotypical and layer-specific projection patterns [31–33]. Alternatively, mean fluorescence intensity is often used to measure overall antibody expression; however, this approach does not account for tissue size nor reveal the number of cells expressing specific markers [22,32,34,35]. This can lead to misinterpretation, as low cell density and high fluorescence signal might resemble high density and weak fluorescence signal when averaged over a large area. By enabling more precise cellular-level statistics, our approach to estimating cell numbers enhances research utilising organoid models of human disease.

Overall, our objectives were to enhance whole-organoid image analysis by providing a way to identify and separate areas of cell death in non-viable regions and quantify cell number and density of non-nucleic antibody markers in viable tissue areas. The resulting analysis workflow incorporated machine-learning-based cell nuclei segmentation implemented via Cellpose v2.2 (Howard Hughes Medical Institute, Ashburn, VA, USA) providing masked images that were further processed in MATLAB (Version R2022b, Mathworks, Natick, MA, USA) via a custom Graphical User Interface (GUI). The analysis workflow was developed to facilitate processing large datasets of tiled and z-series images via progression through a semi-automated step-sequence.

## 2. Materials and Methods

### 2.1. Ethics

Ethics for the project were approved by the Austin Health Human Research Ethics Committee (HREC/16/Austin/472, Melbourne, Australia), and this study was conducted in adherence to the established guidelines set forth by the Austin Hospital, University of Melbourne, and the National Health and Medical Research Council (NHMRC) of Australia.

### 2.2. Human iPSC Model

Organoids were derived from two control cell lines, a hiPSC line derived from a neonate (Cat #WC026i-5807-3, WiCell, Madison, WI, USA) and an embryonic stem cell (ESC) line (Cat #H9 or WA-09, WiCell, Madison, WI, USA). Three batches of cortical organoids were generated from each cell line using the protocol established by

Velasco et al. [12]. Each batch comprised 12 organoids at two developmental stages: 6 were collected on day 120 (4 months) post-induction and 6 on day 180 (6 months).

### 2.3. Immunohistochemistry

At 4 and 6 months post-induction, a minimum of two technical replicates were immersed in 4% paraformaldehyde and incubated for 2 h at 4 °C, and then washed three times in 1x phosphate-buffered saline (PBS), and placed in tissue-Tek O.C.T. Compound (Cat #25608-930); then, they were snap-frozen and stored at −80 °C. Serial cryo-sections were cut at 20 µm thickness (Cat #CM1950; Leica Microsystems, Wetzlar, Germany), collected on SuperfrostPlus glass slides (Cat #I6172PLUS, Thermo Fisher, Waltham, MA, USA) and stored at −80 °C.

Immunohistochemistry was performed according to Yakoub and Sadek [36]. All primary and secondary antibodies are listed in Table 1. Sections were defrosted for 15 min at room temperature (RT), and then blocked using 10% normal goat serum (NGS; Cat #16210064; Invitrogen, Carlsbad, CA, USA) and 0.3% Triton X-100 (Cat#T8787; Sigma-Aldrich, St. Louis, MO, USA) in PBS, for a minimum of 2 h, at RT. Primary antibodies were diluted in an antibody vehicle solution (AVS) of 1% NGS and 0.1% Triton X-100 in PBS), and sections were incubated overnight at 4 °C in the dark. Table 2 details the number of sections included in our analysis. Slides were washed in a solution of 0.05% Tween20 (Cat#655204; Sigma-Aldrich, St. Louis, MO, USA) and PBS and incubated with secondary antibodies (diluted in AVS) for one hour, at RT (see Table 1). A second wash using a solution of 0.05% Tween20 and PBS preceded a 5 min incubation with 6-diamidino-2-phenylindole (DAPI). Two final PBS washes were undertaken then sections were mounted using Invitrogen ProLong Gold Antifade mounting medium (Cat #P36934, Thermo Fisher, Waltham, MA, USA) and covered with Menzel–Glaser glass coverslips (Cat #11911998, #1.5H, Thermo Fisher, Waltham, MA, USA). Slides were subsequently stored at −80 °C until imaged.

**Table 1.** Immunohistochemistry antibodies.

Set	Primary Antibody	Catalogue Number	Dilution	Secondary Antibody	Catalogue Number	Dilution
1	S100β <sup>a</sup>	Sigma-Aldrich S2532	1:500	Goat anti-mouse	Invitrogen A11001	1:300
2	MAP2 <sup>b</sup>	Abcam AB5392	1:200	Donkey anti-chicken	Invitrogen A78951	1:300
3	GABA <sup>c</sup>	Sigma-Aldrich A2052	1:400	Goat anti-rabbit	Invitrogen A32740	1:300
4	Casp-3 <sup>d</sup>	Abcam AB49822	1:1000	Goat anti-rabbit	Invitrogen A21244	1:300
5	TUNEL Assay <sup>e</sup>	Invitrogen C10619	Kit			
1–5	DAPI <sup>f</sup>	Sigma-Aldrich D9452-50MG	1:3000			

<sup>a</sup> S-100 (β-subunit) antibody (S100β). <sup>b</sup> Microtubule-associated Protein 2 (MAP2). <sup>c</sup> Gamma-aminobutyric Acid (GABA). <sup>d</sup> Cleaved—Caspase 3 (Casp3). <sup>e</sup> Terminal deoxynucleotidyl transferase dUTP nick-end labelling (TUNEL Assay Kit). <sup>f</sup> 6-diamidino-2-phenylindole (DAPI) All sets DAPI stained. Abcam, Cambridge, UK; Invitrogen, Carlsbad, CA, USA; Sigma-Aldrich, St. Louis, MO, USA.

**Table 2.** Samples included in quantitative analysis, by primary antibody and time post-induction.

Primary Antibody	4 Months		6 Months		Total	
	No. of Organoids	No. of Sections	No. of Organoids	No. of Sections	No. of Organoids	No. of Sections
S100 $\beta$	5	8	6	16	11	24
MAP2	2	8	6	16	8	24
GABA	6	20	6	20	12	24
Total	13	36	18	52	31	88

To characterise the morphology of the organoids with respect to protein markers indicative of mature expression patterning, three antibodies were used. In mammalian cells, S-100 ( $\beta$ -subunit) (S100 $\beta$ ) protein is predominantly expressed by mature astrocytes and distributed throughout the cytoplasm [37–40]. Microtubule-Associated Protein 2 (MAP2) is a cytoskeletal protein mainly expressed in the soma and dendrites of mature neurons [31]. Gamma-aminobutyric Acid (GABA)ergic neurons are inhibitory neurotransmitters chiefly located in the cytoplasm and dendrites of neurons [41,42]. A total of 88 sections were included in the final analysis, as outlined in Table 2. Additional organoid sections ( $n = 6$ ) were included to verify non-viable cellular and core features using cleaved-caspase-3 antibody and TUNEL assay kit (Table 1).

#### 2.4. Imaging

Images of each organoid slice were acquired using a 20x/0.8NA objective on a Leica THUNDER Imager DMI8 fluorescence microscope (Leica Microsystems, Wetzlar, Germany). Image z-stacks with a z-step size of 0.571  $\mu\text{m}$  and a pixel size of 0.323  $\mu\text{m}$  xy were acquired to ensure adequate sampling in line with recommendations for post-processing using Leica Application Suite X (LASX, version 3.8.1.26810, Leica Microsystems, Germany). A tile scan function was used to rapidly image the entire organoid slice, with a 10% tile overlap. All sections were labelled with DAPI for nuclei segmentation (excitation wavelength used for imaging 391 nm) and either S100 $\beta$  (ex 479 nm), or MAP2 or GABA (ex 554 nm). The images were subject to small volume computational clearing (SVCC) using LASX software [43] before being exported. Settings included feature scale—6000 nm and 30% background scale. In addition, confocal images were also acquired on a subset of organoid slices using an LSM900 scanning confocal microscope 20x/0.8NA (Carl Zeiss Inc., Jena, Germany). Confocal imaging time was considerably longer at approximately 6 h (parameters optimised for Nyquist sampling), versus 10 min on Leica THUNDER (parameters optimised for LASX processing as noted above). Only images acquired using the Leica THUNDER system were used for the analysis workflow development. The Leica THUNDER system presented a significant advantage to achieve high throughput and was used for analysis workflow development as it captured sufficient image quality to segment and analyse antibodies for cell counts. All images were acquired within the Florey Neuroscience Microscopy Facility (The Florey Institute of Neuroscience and Mental Health, Melbourne, VIC, Australia).

#### 2.5. Image Data Analysis

A custom set of MATLAB (Version R2022b, Mathworks, Natick, MA, USA) functions were developed for the purpose of image analysis. These incorporated a range of steps, including tile stitching, nuclei and peri-nucleic antibody segmentation, cell-state characterisation, the identification of the non-viable cell core boundary and applicable calculations. A description of the image analysis workflow is incorporated in the results section outlined below. All analysis scripts are available on request. The analysis workflow was executed on

a Dell PowerEdge R820 Server, equipped with four Intel Xeon E5-4620 processors (2.20 GHz, 16M Cache, 7.2GT/s QPI, Turbo, 8 Core) and supported by a RAM capacity of 512 GB.

### 2.6. Statistical Framework

All statistical analyses and figures relating to the visualisation of data were completed using GraphPad PRISM software (Version 9.5.1, GraphPad Software Inc., La Jolla, CA, USA). Numeric values are reported to three significant figures, and data are presented as mean  $\pm$  standard error of the mean (SEM). To compare groups, multiple *t*-tests with Welch's correction were conducted to account for unequal variances. To compensate for the potential inflation of Type I errors, the False Discovery Rate (FDR)—using the Benjamini–Hochberg method ( $Q = 5\%$ )—was also determined. Comparisons with an FDR-adjusted *p*-value (*q*) less than 0.05 were considered discoveries.

## 3. Results

Cortical organoids obtained from two stem cell control lines were collected at two time points, after 4 and 6 months of differentiation. A workflow for their analysis is presented in Figure 1 and included cortical organoid sectioning (Figure 1A–C), immunohistochemistry and image acquisition (Figure 1D–G). To quantify the cellular composition of organoids, we developed a customised image analysis pipeline.

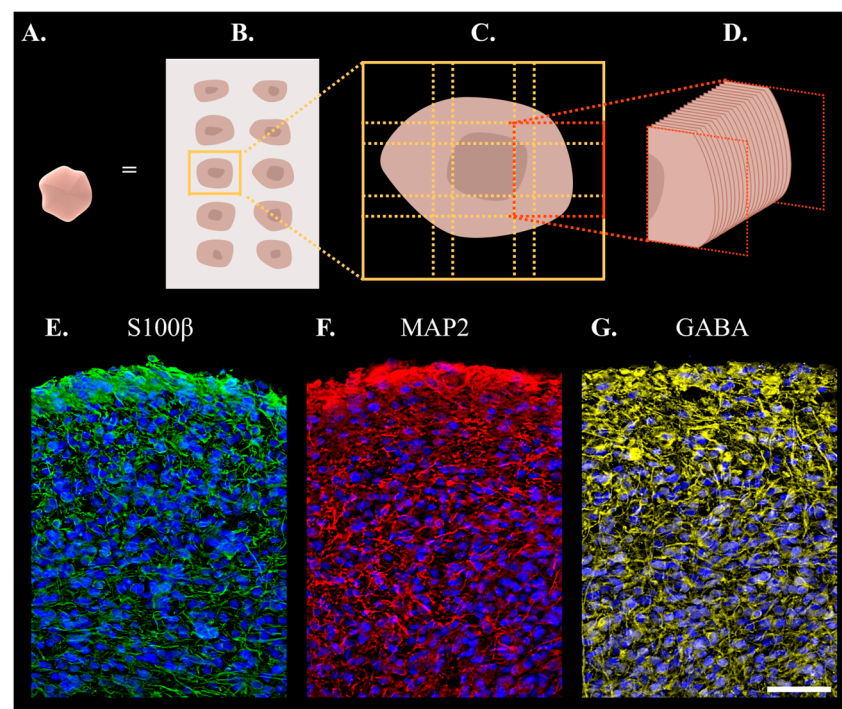


**Figure 1.** Summary of the workflow for organoid analysis included cortical organoid sectioning, immunohistochemistry and image acquisition. (A) Single organoid, representing one of 31 analysed. (B) Schematic of a slide with ten organoid sections, nine tiles were imaged per organoid section. (C) Tiled images shown across a single section in the x-y plane (dotted lines). (D) Individual tile illustrates (3D) z-stack acquired for all images. (E–G) Example immuno-histochemistry for the organoid sections: (E) staining with DAPI (blue) and S100 $\beta$  (green), marking mature astrocytes; (F) DAPI (blue) and MAP2 (red), indicating mature neurons; (G) DAPI (blue) and GABA (yellow), highlighting inhibitory neurons. 6-diamidino-2-phenyl-indole (DAPI); S-100 calcium-binding  $\beta$ -subunit (S100 $\beta$ ); Microtubule-associated Protein 2 (MAP2); Gamma-aminobutyric Acid (GABA). Scale 50  $\mu$ m.

### 3.1. 3D Analysis of Organoid Slices

As previously outlined, fluorescently labelled cortical organoid slice images were captured using Leica Application Suite (LASX). To preserve the inherent 3D tissue structure, image processing of z-stacks, which comprised 2D tiled images taken across the x–y plane, were reconstructed as a 3D spatial model of the organoid sections. Automated analysis of the entire organoid section was performed to capture the intrinsic structural heterogeneity and provide a more representative sampling approach to quantifying organoid morphological features such as cell density, viability, and antibody expression across developmental stages.

### 3.2. Identification of Tissue Boundaries

The outer boundary of each organoid was identified automatically to define the tissue margins (Figure 2A). Tissue artefacts such as tears and folds were also detected and excluded from further analysis (Figure 2B). This process involved generating a binary image by stitching tiled images into a composite overview of the section, applying a threshold using Otsu's method, and performing morphological closing to smooth edges and eliminate small internal holes. Figure 2D illustrates the refined viable region, showing only the viable cells remaining for analysis, as detailed in the next section.

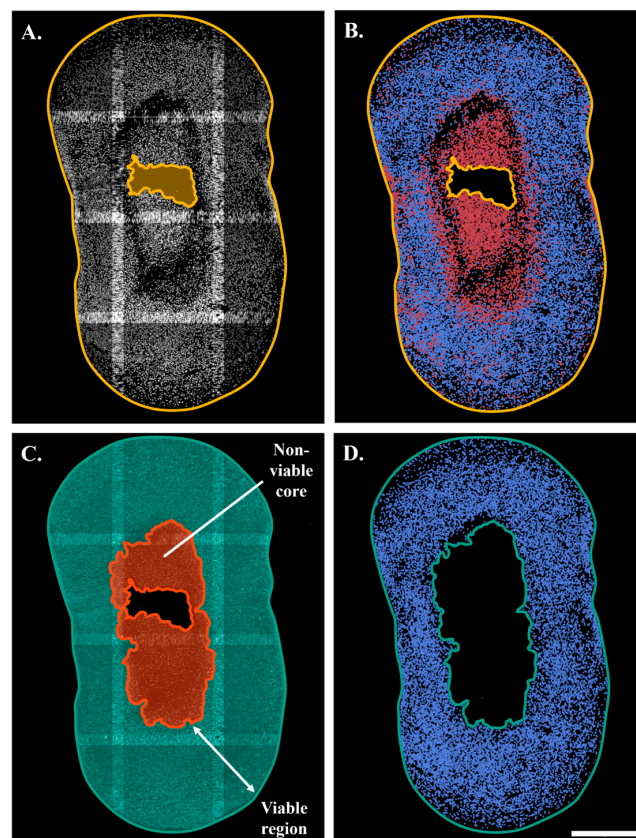


**Figure 2.** Method for processing tiled images of cortical organoid section boundary refinement. (A) Composite of a  $4 \times 3$  tile grid merging DAPI and marker channels, showing the outer boundary of the section and a section tear (yellow). (B) Schematic of the entire section, illustrating the outer boundary and section tear (yellow), with viable cells (blue), and non-viable cells (red). (C) Schematic of the non-viable core (red), which was excluded from analysis and viable region (green) in a cortical organoid section. The viable region represents the area between the outer boundary of the section and the core boundary. (D) Schematic of the viable region, with the outer and inner boundaries (green), and viable cells only (blue). Scale 400  $\mu\text{m}$ .

### 3.3. Nuclei Segmentation

The analysis workflow enabled accurate segmentation of nuclei (Figure 3) and provided the organoid cell counts. Nuclei segmentation was based on DAPI-labelling. Algorithm selection was a crucial step, as tightly packed cellular structures within cortical organoids can be highly confounding for cell counts. Several tools for 3D object segmentation were explored, including Imaris (v9.9, Oxford Instruments, Zurich, Switzerland), CellProfiler (v4.2.5, Broad Institute, Cambridge, MA, USA), Cellpose v2.2 and Image J v1.54f. [44]; example segmentation results are shown in Figure 3A–D. Each package was evaluated for speed, reliability, and ability to adapt to a heterogenous sample. Compared to other packages tested, the machine learning framework utilised by Cellpose v2.2 demonstrated proficiency when faced with complex and varied samples and was embedded into the analysis workflow. Three-dimensional segmentation was completed using the nuclear model with a minimum mask size of 15 pixels and an initial object diameter of 30.8 pixels. Anisotropy was defined as the ratio of z-step size ( $\mu\text{m}$ ) to pixel size ( $\mu\text{m}$ ) for each image. The resulting segmented DAPI-labelled images, outputted as 16-bit Tag Image File Format (.tif) files, provided a basis for subsequent analyses within the workflow.

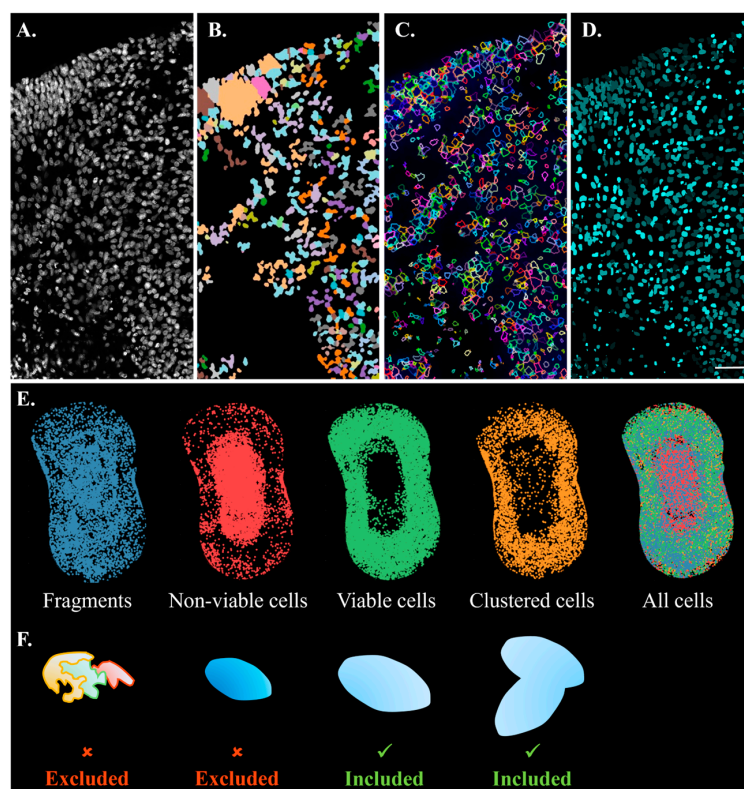


**Figure 3.** Segmentation and classification of DAPI-labelled cell nuclei in cortical organoid sections. (A–D) Comparative segmentation tools of DAPI-labelled cell nuclei in a cortical organoid section. (A) Original grayscale image. (B) Segmentation by CellProfiler v4.2.5, with distinct colours marking individual nuclei. (C) Segmentation by Imaris v9.9, highlighting the boundaries of nuclei in distinct colours. (D) Segmentation by Cellpose v2.2, with nuclei identified in cyan; pixel intensity indicates individual cells. (E) Panel of two-tiered GMM classification of cell nuclei post-segmentation. (Left to right) Initial classification distinguishes small volume fragments or improperly segmented cells (blue). Subsequent analysis categorises cells as non-viable (red) and viable (green). Example large volume or clustered cells (yellow) and overlay of all cell classifications (colour merge). (F) Panel illustrates individual segmented nuclei based on GMM classification (above), including (left-right) fragmented and non-viable nuclei, which were excluded from analysis, and viable and clustered nuclei, which were included. Gaussian Mixture Model (GMM). Scale 50  $\mu\text{m}$  (A–D).

### 3.4. Cell-State Classification

Nuclei were then classified into four distinct groups: cell fragments, non-viable, viable, and clustered or dividing cells (Figure 3E). This classification was initially based on nuclei volume, calculated from the segmented images outputted by Cellpose v2.2. The volumes were fitted to a Gaussian Mixture Model (GMM) with three components (Figure 3E). The GMM distinguished between very small volumes ( $\bar{x} = 8.57 \mu\text{m}^3$ ), representing cell fragments or improperly segmented nuclei; moderate volumes, representing single cells; and large volumes ( $\bar{x} = 548 \mu\text{m}^3$ ), corresponding to dividing or clustered cells. Fragments were excluded from further analysis (Figure 3F).

DAPI-stained nuclei of apoptotic or dead cells typically exhibit lower volumes and higher fluorescent intensities due to condensed DNA and cytoplasm compared to their viable counterparts [45,46]. These features were leveraged for the application of a second GMM, used to classify the group of moderate volumes as either viable ( $\bar{x} = 219 \mu\text{m}^3$ ) or non-viable ( $\bar{x} = 149 \mu\text{m}^3$ ; apoptotic/dead) cells. The estimated mean volumes of nuclei within the non-viable and viable regions were provided as initial parameters for the GMM, which incorporated both volume and intensity data. For clarity, dying and dead cells are described as non-viable for the remainder of the report. The sequential application of GMMs resulted in each nucleus being allocated to one of the four final groups (Figure 3F).

The results obtained for the nuclei feature detection and cell classification were confirmed using a separate set of organoid sections containing a non-viable cell core. To identify the apoptotic pathway, we included cleaved-Caspase-3 antibody and Terminal deoxynucleotidyl transferase dUTP nick-end labelling (TUNEL) assay ( $n = 3$  each). The classification of non-viable cells, at high density within the organoid core, was confirmed by both cleaved-Caspase-3 antibody (Supplementary Figure S1A–C) and TUNEL assay (Supplementary Figure S1D–F), which showed positive staining concentrated within the organoid core. To verify, at a cellular level, non-viable versus viable cells, the mean fluorescence intensity and diameter of nuclei for either DAPI/TUNEL-positive (non-viable) or DAPI<sup>+</sup>/TUNEL<sup>-</sup> (viable) cells was calculated using Image J ( $n = 20$  each). Nuclei intensity plots were obtained using a line segment of  $1 \mu\text{m}$  width (Supplementary Figure S1H,I). Classification of non-viable cells using DAPI-nuclei staining confirmed that a small diameter ( $\leq 6 \mu\text{m}$ ) and high signal intensity nuclei were TUNEL-positive, while lower-signal-intensity DAPI<sup>+</sup> cell nuclei ( $>6 \mu\text{m}$ ) were TUNEL-negative, consistent with the viable cell classification used in the analysis workflow.

### 3.5. Identification of Non-Viable and Viable Regions

To obtain organoid measurements including, for example, the core size and cell density, the analysis workflow was developed to automatically delineate viable and non-viable areas.

#### 3.5.1. Non-Viable Regions

Automatically demarcating the non-viable cell core is challenging due to the intermingling of dead and viable cells throughout the organoid. This phenomenon is underpinned by several factors, including the gradient of nutrient diffusion, natural rates of cell death, incurred damage, and variations in hypoxia resistance [24,47]. To demarcate the presence of a core and approximate core boundary, a novel protocol was applied. Binary masks were generated of the non-viable and viable nuclei in each segmented image tile, and Maximum Intensity Projections (MIPs) were created for each of the two masks. Local cell densities were then calculated for both the non-viable and viable MIPs using a sliding window convolution. The necrotic density map was then subtracted from the viable density map, and regions with a high ratio of non-viable cells were identified using a threshold-based

method, marking the necrotic core. Finally, morphological smoothing and hole-filling operations were applied to refine the necrotic core boundary.

### 3.5.2. Viable Region

The viable regions in all samples were calculated from the total area of the section, delineated by the outer boundary, minus the region containing the non-viable cell core (example shown in Figure 2C,D).

### 3.5.3. Non-Viable Cells Within the Viable Region

Nuclei centroids positioned within the viable region of the samples were extracted for analysis. The relative frequency of cell death within the viable region was subsequently calculated as the percentage of non-viable cells relative to the total number of cells within the viable region.

### 3.6. Estimation of Antibody Positive Cell Count

This section outlines the portion of the analysis workflow used to quantify the number of cells expressing S100 $\beta$ , MAP2, and GABA antibodies. As a brief overview, first, the antibody-positive voxels were identified by thresholding the antibody-labelled images. Next, a peri-nuclear shell was obtained by dilating the DAPI-mask corresponding to each viable cell nuclei. Finally, the percentage of antibody-positive voxels within the shell was measured. A schematic to distinguish the spatial classification of nuclei and peri-nuclear markers is given in Figure 4A–D for this part of the analysis workflow and described in detail below.

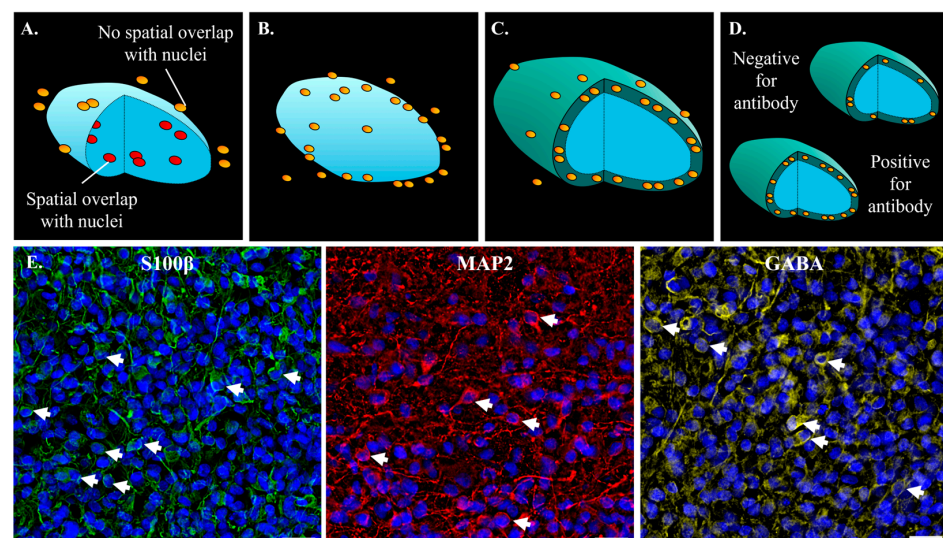


**Figure 4.** Delineation and classification of peri-nuclear protein distribution. (A) Schematic representation of a cell nucleus (blue) with nuclear proteins (red) and extranuclear proteins (yellow). (B) Illustration of a DAPI-labelled cell nucleus (blue) segmented using the Cellpose algorithm, with antibody-positive pixels (yellow) detected in the surrounding area. (C) Visualisation of the peri-nuclear region (green), defined by applying a dilation algorithm to the boundaries of the segmented nucleus. Antibody-positive pixels located within this region are highlighted (yellow). (D) Classification criteria for cell nuclei based on antibody presence: nuclei were deemed positive when their peri-nuclear shell contained the minimum cutoff value for the antibody marker; otherwise, they were deemed as negative. (E) Examples of antibody-positive cells visually classified for markers S100 $\beta$ , MAP2 and GABA. Arrows indicate cells identified as positive based on the extent of peri-nuclear antibody label. 6-diamidino-2-phenylindole (DAPI); S-100 ( $\beta$ -subunit) antibody (S100 $\beta$ ); Microtubule-associated Protein 2 (MAP2); Gamma-aminobutyric Acid (GABA). Scale 20  $\mu$ m.

### 3.6.1. Antibody Positive Voxels

The measurement of antibody expression involved the application of a cutoff to the antibody image. An adaptive threshold was selected according to Otsu's three-class method, a classification method based on intensity, with the middle class assigned to the background. This is an established approach that was selected for its robustness when applied to antibody-stained images with multi-modal characteristics [48,49]. The result was a binary image of all voxels identified as positive for the antibody, from which the percentage volume occupied by the antibody was calculated.

### 3.6.2. Delineation of Peri-Nucleic Region

The masked images of the segmented nuclei were dilated using a spherical structuring element three voxels ( $\sim 1 \mu\text{m}$ ) in diameter (Figure 4A,B). This resulted in a mask of the three-dimensional "shell" around the nuclei, or peri-nucleic region (Figure 4C).

### 3.6.3. Identification of Antibody-Positive Cells

In order to distinguish antibody "positive" cells from antibody "negative" ones and to account for cells whose nuclei were positioned in close proximity to the antibody labelling expressed by other cells, a cutoff method was applied. The cutoff value was guided by two experts in the domain, who visually classified cells from a single 3D tile for each antibody as either positive or negative (Figure 4D). In Figure 4E are example images of the antibody labelling highlighting cells which were manually identified as positive. Positive cells were defined as those with a 3D fluorescence signal surrounding a DAPI-labelled nucleus. The mean percentage of antibody signal within the peri-nucleic shell of visually identified positive cells was calculated and used to set the minimum cut-off value for classifying antibody positive cells in the image processing workflow. The thresholds were established as 31.5% for GABA, 23.2% for MAP2, and 10.4% for S100 $\beta$ , with any cell exceeding the respective cut-off considered positive. The percentage of antibody-positive cells within the viable regions were then calculated. The spatial distribution of antibody-positive and antibody-negative cells, including their x and y coordinates, was also calculated, as visualised in Figure 5.

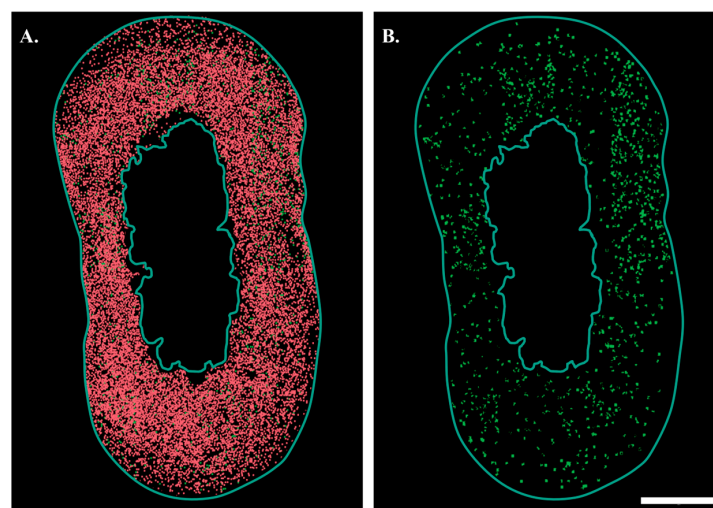


**Figure 5.** Schematic representation of antibody-positive and -negative cells within the viable region of cortical organoid sections. (A) The viable region, defined by the outer and inner boundaries (teal). Cells identified as antibody-positive are shown in green, while antibody-negative cells are shown in red. (B) The viable region with the outer and inner boundaries (teal), showing only antibody-positive cells (green). Scale 400  $\mu\text{m}$ .

### 3.7. Volume Estimation

To estimate the volume of the slice, we combined the x–y pixel map with the z-coordinates of the segmented nuclei. This was performed as a heatmap spatially averaging this information across sub-regions,  $200 \times 200$  pixels in size. Overlaying the pre-defined inner boundaries of the non-viable core and outer boundary of the organoid slice, their volumes could be estimated.

### 3.8. Temporal Analysis of Organoid Morphology and Maturation

The analysis workflow was applied to measure the developmental trajectory of control cortical organoids between 4 and 6 months post-induction. Measurements included the volume of the non-viable core, cell densities, and three cell populations, composed of astrocytes (S100 $\beta$ ) and neurons, which included all neurons (MAP2) and GABAergic interneuron sub-type. In total, 88 sections from 31 organoids were analysed, as outlined in Table 2.

#### 3.9. A Proportional Decrease in Non-Viable Cells Was Observed from 4 to 6 Months Post-Induction

The structural health of the organoids was assessed by the relative size of the non-viable cell core. A non-viable cell core was identified in 40 (86.9%) of those sampled at 4 months post-induction and 32 (61.5%) of those sampled at 6 months post-induction. There was no change in the total volume of the organoid sections examined over time (Figure 6A). However, analysis of the volume of the non-viable core as a percentage of the total volume was significantly reduced with a mean of 26.4% versus 18.8% at 4 month and 6 months post-induction, respectively (Figure 6B); difference = 7.6%, SE of difference = 3.1%,  $t(62.9) = 2.5$ ,  $p = 0.0168$ ,  $q = 0.0176$ .

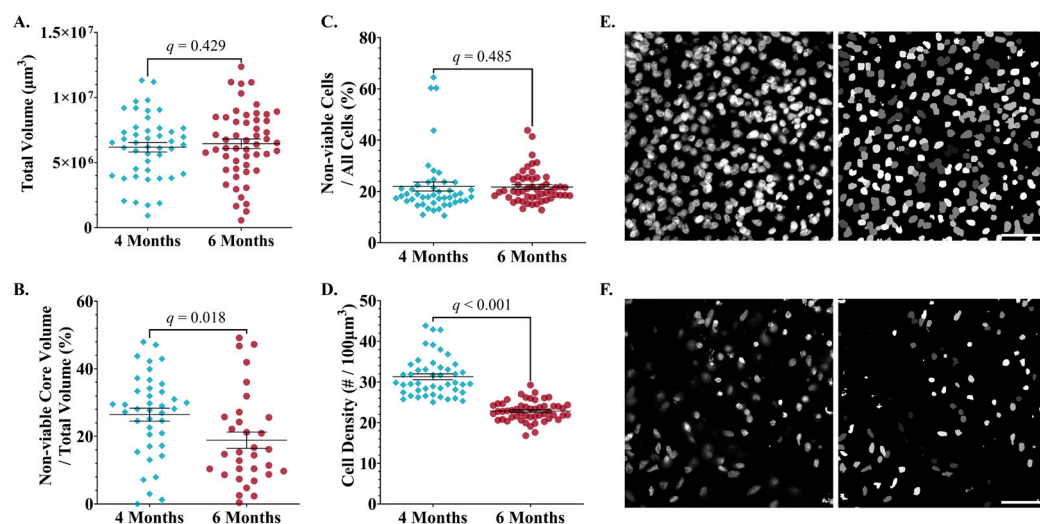


**Figure 6.** hESC-derived cortical organoid morphology features assessed at 4- and 6 months post-induction using the image analysis workflow. Blue diamonds represent organoid sections at 4 months and red circles at 6 months. Error bars SEM. Results refer to Welch's  $t$ -tests performed with Benjamini–Hochberg correction ( $Q = 0.05$ ). (A) No discovery was made regarding differences in total section volume. (B) A discovery was made as to the volume of the non-viable core as a percentage of total section volume, with a reduction observed at 6 months post-induction. (C) No discovery was made in relation to the percentage of cells within the viable region that were non-viable. (D) Overall cell density within the viable region was reduced at 6 months compared to 4 months post-induction. (E) Representative DAPI-stained cortical organoid section at 4 months post-induction. Left: Single-plane

raw image of nuclei. Right: Processed image showing segmented nuclei identified by the Cellpose algorithm, with individual nuclei displayed in greyscale. (F) Representative DAPI-stained cortical organoid section at 6 months post-induction. Left: Single-plane raw image of nuclei. Right: Processed image showing segmented nuclei identified by Cellpose. The reduced density of segmented nuclei at 6 months reflects the decrease in cell density quantified in panel (D). Standard Error Mean (SEM). Scale 40  $\mu\text{m}$ .

The cellular health of the organoids was evaluated by calculating the percentage of non-viable cells relative to the total cell count within the viable region of the samples. No discovery was made when comparing mean ratios at 4 months ( $\bar{x} = 22.0\%$ ) and 6 months ( $\bar{x} = 21.8\%$ ) post-induction (Figure 6C); Difference = 0.19%, SE of difference = 3.1,  $t(66.26) = 0.096$ ,  $p = 0.924$ ,  $q = 0.485$ .

### 3.10. Cell Density in Cortical Organoids Was Higher at 4 Months Versus 6 Months Post-Induction

Cell density was utilised to measure cell proliferation and evaluated in the viable region of cortical organoids. The viable cell density in this region was higher at 4 months ( $\bar{x} = 31.3$  cells/ $100 \mu\text{m}^3$ ) compared to 6 months ( $\bar{x} = 22.8$  cells/ $100 \mu\text{m}^3$ ) post-induction (Figure 6D–F); Difference = 8.4, SE of difference = 0.794,  $t(64.4) = 10.6$ ,  $p < 0.000001$ ,  $q = < 0.000001$ .

### 3.11. Quantifying Expression of Astrocyte and Neuronal Markers

#### 3.11.1. S100 $\beta$ Expression Was Unchanged from 4 to 6 Months Post-Induction

The maturation of individual astrocytes was assessed using the ratio of S100 $\beta$ -positive cells to all viable cells. At 4 months the mean percentage of S100 $\beta$ -positive cells was 11.1%, compared to 13.6% at 6 months post-induction (Figure 7A). No discovery was made with this comparison; Difference =  $-2.5\%$ , SE of difference = 1.7,  $t(25.8) = 1.4$ ,  $p = 0.162$ ,  $q = 0.346$ . The mean density of S100 $\beta$ -positive cells was also similar at 4 ( $\bar{x} = 2.9$  cells/ $100 \mu\text{m}^3$ ) and 6 months ( $\bar{x} = 2.5$  cells/ $100 \mu\text{m}^3$ ) post-induction (Figure 7B); Difference = 0.376, SE of difference = 0.404,  $t(31.7) = 0.93$ ,  $p = 0.36$ ,  $q = 0.378$ .

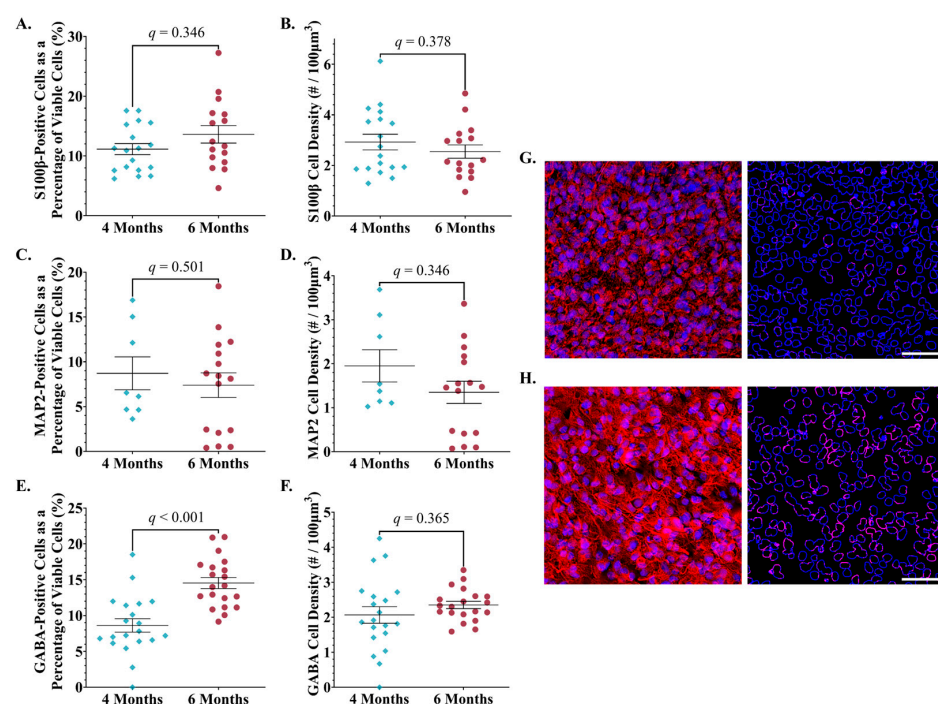


**Figure 7.** Temporal analysis of percentage and density of marker positive cells in ESC-derived cortical organoids. Blue diamonds represent sections at 4 months and red circles at 6 months. Error bars SEM.

Results refer to Welch's *t*-tests performed with a Benjamini–Hochberg correction ( $Q = 0.05$ ). (A–D) No discoveries were made when comparing the percentage of cells positive for either S100 $\beta$  or MAP2 within the viable region, nor when considering positive cell density. (E) A discovery was made as to the percentage of cells positive for GABA within the viable region, with an increase observed at 6 months post-induction. (F) A discovery was not observed as to the density of GABA-positive cells. (G) Representative image of a cortical organoid section at 4 months post-induction, stained for DAPI (blue) and GABA (red). Left: Single-plane raw image. Right: Peri-nuclear regions showing pixels without GABA staining (blue) and pixels positive for GABA (pink). (H) Representative image of a cortical organoid section at 6 months post-induction, stained for DAPI (blue) and GABA (red). Left: Single-plane raw image. Right: Peri-nuclear regions showing GABA-negative pixels (blue) and GABA-positive pixels (pink). The increased proportion of GABA-positive cells at 6 months aligns with the quantitative findings shown in panel (E). Standard error mean (SEM). Scale 40  $\mu\text{m}$ .

### 3.11.2. No Change in MAP2 Expression from 4 to 6 Months Post-Induction

The temporal assessment of neuron maturation was made using the percentage of MAP2-positive cells in organoids at 4 and 6 months. As a proportion of all viable cells, MAP2-positive cells showed a decrease from 8.7% to 7.4% from 4 to 6 months post-induction, respectively, which did not result in a discovery (Figure 7C); difference = 1.3, SE of difference = 2.3,  $t(14.8) = 0.577$ ,  $p = 0.573$ ,  $q = 0.502$ . Similarly, no discovery was made in relation to the differences in density of MAP2-positive cells from 4 ( $\bar{x} = 1.95$  cells/100  $\mu\text{m}^3$ ) to 6 months ( $\bar{x} = 1.3$  cells/100  $\mu\text{m}^3$ ) post-induction (Figure 7D); difference = 0.602, SE of difference = 0.445,  $t(13.8) = 1.35$ ,  $p = 0.198$ ,  $q = 0.346$ .

### 3.11.3. The Proportion of GABA-Positive Cells Increased, but No Change in GABA-Positive Cell Density 6 Months Post-Induction

The differentiation of GABAergic neurons was assessed by the percentage of GABA-positive cells at 4 ( $\bar{x} = 8.6\%$ ) and 6 months ( $\bar{x} = 14.5\%$ ) post-induction. A discovery revealed a significant increase in the proportion of GABA-positive cells over time (Figure 7E,G,H); difference =  $-5.9\%$ , SE of difference = 1.2,  $t(36.8) = 4.9$ ,  $p = 0.00002$ ,  $q = 0.0001$ . An increase in the density of GABA-positive cells was observed between 4 ( $\bar{x} = 2.07$  cells/100  $\mu\text{m}^3$ ) and 6 months ( $\bar{x} = 2.4$  cells/100  $\mu\text{m}^3$ ) post-induction, though no discovery was made regarding this change (Figure 7F); difference =  $-0.286$ , SE of difference = 0.258,  $t(26.0) = 1.1$ ,  $p = 0.278$ ,  $q = 0.365$ .

## 4. Discussion

We have established an image analysis workflow to serve as a standardised method for the assessment of organoid viability and cytoarchitecture. The workflow was tested on a dataset of more than 1.5 million cells and demonstrated remarkable efficacy in identifying specified cell types and states, as well as providing temporal and spatial information when applied to cortical organoid development.

To enhance our analysis beyond single-plane imaging, we captured the entire organoid slice in 3D, revealing details of the cellular organisation that traditional maximum intensity projection methods omit. Additionally, our automated analysis of the complete section enabled us to explore the regional diversity within the organoids across each group. This comprehensive approach provided deeper insights into cellular features such as density, viability, and antibody expression at various developmental stages.

To implement high-throughput imaging, we utilised a widefield fluorescence microscope system. The advantage of this imaging approach was that it provided 3D acquisition of entire sections in a fraction of the time needed for confocal microscopy when using similar acquisition parameters. The widefield system adequately captured the nuclear marker and the peri-nuclear environment, which were the primary focus of our analyses.

These findings suggest that widefield microscopy is a suitable alternative when a balance between resolution and higher acquisition speed is required.

The Leica Thunder system has three computational clearing algorithms available. Here, we implemented Small Volume Computational Clearing (SVCC). This algorithm applies adaptive deconvolution before removing unwanted background [43]. Image datasets captured using this method provided sufficient cellular detail to facilitate automated cell counts. The resultant analysis workflow was designed to process widefield 3D image tiles; however, it could also be applied to any fluorescence image datasets for example, optically sectioned whole tissue samples using light-sheet microscopy [19,22]

At present, research using organoid models lacks a well-defined benchmark for 'normal' growth and development. We have established an "in-house" method to benchmark the elected organoid protocol tailored to the specific needs of cytoarchitectural analysis, an exercise critical to identify, interpret and compare deviations between control and disease models.

The analysis workflow's initial task was to quantify non-viable and viable cells using the nuclear label. Non-viable or necrotic cells have previously been identified in organoid image-based studies by their higher fluorescence intensity and smaller diameter nuclei in comparison to functional cells [50–52]. While previous studies focused on a single attribute, we adopted a more comprehensive approach by implementing a two-tiered Gaussian Mixture Model that analyses both volume and intensity. This approach allowed for more complex stratification of candidate cells. We show that nuclei classified using the integrated approach as non-viable cells was confirmed using cleaved-caspase 3 and TUNEL staining, consistent with previous reports [12,35,46,53] The approach also allowed automatic delineation of the non-viable core boundary from the viable region, which was a significant advancement.

To evaluate organoid viability, the nucleic viability classifications were applied to obtain quantitative "in-house" assessment of cortical organoids including the non-viable core volume and percentage non-viable cells in the viable region. We found a significant decrease in the volume of the non-viable core between 4 and 6 months post-induction. In contrast to this finding, previous research has proposed that the "dead cell" core increases over time, caused by the limited diffusion of oxygen and nutrients from the organoid surface in the avascular model [14,47,54]. To interrogate the current finding, we quantified two additional factors likely to affect core size including the densities of viable and dead cells within the viable region. Our results indicated a reduced viable cell density within the viable region, from 4 to 6 months. Second, we found the viable region showed a decreased number of non-viable or dead cells from 4 to 6 months, which is consistent with reported cell death rates in cerebral organoids plateauing as they near synaptic maturity [55]. Taken together, these results indicate diffusion rates across the viable region may be higher at 6 months. Additional transcriptional analysis would help to determine whether changes in gene expression involved in aerobic respiration and apoptotic genes are consistent with current findings [56]. Overall, the results suggest that evaluating the non-viable core and viable region's growth at a cellular level can help to understand how these factors might influence the health and development of cortical organoids in control and disease models.

To quantify the number of protein labelled cells, the analysis workflow was designed to capture each cell's peri-nuclear protein expression level. Micro-structure in mature cortical organoids is complex in terms of both tightly packed heterogeneous cells and sub-cellular protein expression patterns, which make automating and obtaining cell counts for non-nucleic markers challenging. Therefore, our approach was to use each viable cell's DAPI-mask and create a dilated 3D volume or peri-nuclear shell.

With respect to quantifying organoid maturation, our assessment of between 4 and 6 months post-induction showed no significant differences in S100 $\beta$  expression, indicating that astrocytic maturation remains stable throughout this period. This finding was somewhat unexpected, given the literature describing a continual increase in proliferation from the beginning of astrogenesis in cerebral models [12,21,57,58]. Two possible explanations for these findings arise: first, it may be that the rate of astrocytic maturation is variable over time and that this variation has not previously been captured; second, although widely applied as a measure of astrocytic maturation, S100 $\beta$  is not expressed in all mature astrocytes [40,59]. Therefore, quantitative changes in maturation based on S100 $\beta$  may be limited, and additional markers like glial fibrillary acidic protein (GFAP) could provide further insight.

The percentage of all cells characterised as mature MAP2 positive neurons was similar from 4 to 6 months post-induction, while the percentage of GABAergic neurons was significantly increased. These findings suggest a potential shift in the neuronal population towards GABAergic neurons, consistent with previous studies that revealed a shift occurs at approximately 3–6 months post-induction [9,12]. These observations emphasise how the image analysis workflow can be used to evaluate cell number in models of neurodevelopmental disorders, particularly where GABAergic interneurons are thought to have a significant impact [9,60,61].

Future application of the image analysis workflow could include machine learning development. By capturing spatial and single-cell-level information from sample images, including protein signatures, the workflow can also be expanded to incorporate the cells' molecular profile. This spatial mapping enables detailed profiling of each cell across large replicate datasets. Such advancements align with proposed developments in machine learning, where immunohistochemistry analysis of patient-derived organoids could serve as a valuable tool for personalised drug screening platforms [62,63].

In conclusion, we established a method to benchmark the preferred organoid protocol “in-house”. Functionalities were built into a single, customizable script and incorporated changes to improve their theoretical robustness, tailored to the specific needs of cytoarchitectural cortical organoid analysis. Implementing the current workflow would help laboratories to establish their own benchmark; a critical exercise for identifying, interpreting and comparing deviations across disease and control models. Furthermore, we hope that implementing this workflow in other laboratories using similar differentiation protocols will generate quantifiable outcomes, ultimately establishing a benchmark based on the approach itself rather than being limited to a specific lab.

**Supplementary Materials:** The following supporting information can be downloaded at: <https://www.mdpi.com/article/10.3390/organoids4010001/s1>, Figure S1: Confirming cell state classification using Caspase-3-cleaved and TUNEL assay.

**Author Contributions:** Conceptualization, S.H., K.R., T.J.K., P.K. and S.M.; methodology, S.H., K.R., P.K., T.J.K., C.A.C. and A.S.; validation, S.H. and K.R.; formal analysis, S.H. and K.R.; investigation, S.H., K.R. and T.J.K.; resources and funding, S.M. and S.P.; software, S.H. and T.J.K.; supervision, T.J.K., K.R., P.K. and S.M.; data curation, S.H. and T.J.K.; writing—original draft, S.H. and K.R.; writing—review & editing, S.H., K.R., T.J.K., P.K., C.A.C., A.S., S.P. and S.M. All authors have read and agreed to the published version of the manuscript.

**Funding:** This study was supported by National Health and Medical Research Council (NHMRC) Program grant (10915693) to S.P., and Ideas grant (2029883) to S.M., Medical Research Future Fund (MRFF) Accelerated Research Stem Cell grant to S.P. and S.M. and MRFF Genomic Health Futures Mission Project Grant (GHFMCDI000002) to S.M. and S.P. and project funding by RogCon, Inc.

**Institutional Review Board Statement:** The study was conducted in accordance with the Declaration of Helsinki, and approved by the Austin Health Human Research Ethics Committee (HREC/16/Austin/472, Melbourne, Australia).

**Data Availability Statement:** The code and GUI are available on request.

**Acknowledgments:** The Florey Institute of Neuroscience and Mental Health acknowledges the strong support from the Victorian Government and in particular the funding from the Operational Infrastructure Support Grant.

**Conflicts of Interest:** Steven Petrou is an equity holder of RogCon, Inc. and Praxis Precision Medicine, Inc., Cambridge, MA, USA.

## References

1. Kim, J.; Koo, B.-K.; Knoblich, J.A. Human organoids: Model systems for human biology and medicine. *Nat. Rev. Mol. Cell Biol.* **2020**, *21*, 571–584. [[CrossRef](#)] [[PubMed](#)]
2. Di Lullo, E.; Kriegstein, A.R. The use of brain organoids to investigate neural development and disease. *Nat. Rev. Neurosci.* **2017**, *18*, 573–584. [[CrossRef](#)]
3. Takahashi, K.; Tanabe, K.; Ohnuki, M.; Narita, M.; Ichisaka, T.; Tomoda, K.; Yamanaka, S. Induction of pluripotent stem cells from adult human fibroblasts by defined factors. *Cell* **2007**, *131*, 861–872. [[CrossRef](#)]
4. Qian, X.; Nguyen, H.N.; Song, M.M.; Hadiono, C.; Ogden, S.C.; Hammack, C.; Yao, B.; Hamersky, G.R.; Jacob, F.; Zhong, C.; et al. Brain-Region-Specific Organoids Using Mini-bioreactors for Modeling ZIKV Exposure. *Cell* **2016**, *165*, 1238–1254. [[CrossRef](#)]
5. Centeno, E.G.Z.; Cimarosti, H.; Bithell, A. 2D versus 3D human induced pluripotent stem cell-derived cultures for neurodegenerative disease modelling. *Mol. Neurodegener.* **2018**, *13*, 27. [[CrossRef](#)] [[PubMed](#)]
6. Koo, B.; Choi, B.; Park, H.; Yoon, K.J. Past, Present, and Future of Brain Organoid Technology. *Mol. Cells* **2019**, *42*, 617–627. [[CrossRef](#)]
7. Mao, M.; Mattei, C.; Rollo, B.; Byars, S.; Cuddy, C.; Berecki, G.; Heighway, J.; Pachernegg, S.; Menheniott, T.; Apted, D.; et al. Distinctive In Vitro Phenotypes in iPSC-Derived Neurons from Patients with Gain- and Loss-of-Function SCN2A Developmental and Epileptic Encephalopathy. *J. Neurosci.* **2024**, *44*, e0692232023. [[CrossRef](#)]
8. Ovchinnikov, D.A.; Jong, S.; Cuddy, C.; Scheffer, I.E.; Maljevic, S.; Petrou, S. Generation of an iPSC line (FINi001-A) from a girl with developmental and epileptic encephalopathy due to a heterozygous gain-of-function p.R1882Q variant in the voltage-gated sodium channel Nav1.2 protein encoded by the SCN2A gene. *Stem Cell Res.* **2023**, *71*, 103179. [[CrossRef](#)] [[PubMed](#)]
9. Paulsen, B.; Velasco, S.; Kedaigle, A.J.; Pignoni, M.; Quadrato, G.; Deo, A.J.; Adiconis, X.; Uzquiano, A.; Sartore, R.; Yang, S.M.; et al. Autism genes converge on asynchronous development of shared neuron classes. *Nature* **2022**, *602*, 268–273. [[CrossRef](#)] [[PubMed](#)]
10. Urresti, J.; Zhang, P.; Moran-Losada, P.; Yu, N.-K.; Negraes, P.D.; Trujillo, C.A.; Antaki, D.; Amar, M.; Chau, K.; Pramod, A.B.; et al. Cortical organoids model early brain development disrupted by 16p11.2 copy number variants in autism. *Mol. Psychiatry* **2021**, *26*, 7560–7580. [[CrossRef](#)] [[PubMed](#)]
11. Camões dos Santos, J.; Appleton, C.; Cazaux Mateus, F.; Covas, R.; Bekman, E.P.; da Rocha, S.T. Stem cell models of Angelman syndrome. *Front. Cell Dev. Biol.* **2023**, *11*, 1274040. [[CrossRef](#)] [[PubMed](#)]
12. Velasco, S.; Kedaigle, A.J.; Simmons, S.K.; Nash, A.; Rocha, M.; Quadrato, G.; Paulsen, B.; Nguyen, L.; Adiconis, X.; Regev, A.; et al. Individual brain organoids reproducibly form cell diversity of the human cerebral cortex. *Nature* **2019**, *570*, 523–527. [[CrossRef](#)]
13. von Bartheld, C.S.; Bahney, J.; Herculano-Houzel, S. The search for true numbers of neurons and glial cells in the human brain: A review of 150 years of cell counting. *J. Comp. Neurol.* **2016**, *524*, 3865–3895. [[CrossRef](#)]
14. Brémond, C.; Chane, C.; Clouchoux, C.; Histace, A. Recent Trends and Perspectives in Cerebral Organoids Imaging and Analysis. *Front. Neurosci.* **2021**, *15*, 629067. [[CrossRef](#)]
15. Kassis, T.; Hernandez-Gordillo, V.; Langer, R.; Griffith, L.G. Orgaquant: Human intestinal organoid localization and quantification using deep convolutional neural networks. *Sci. Rep.* **2019**, *9*, 12479. [[CrossRef](#)] [[PubMed](#)]
16. Gritti, N.; Lim, J.L.; Anlaş, K.; Pandya, M.; Aalderink, G.; Martínez-Ara, G.; Trivedi, V. MORGAna: Accessible quantitative analysis of organoids with machine learning. *Development* **2021**, *148*, dev199611. [[CrossRef](#)] [[PubMed](#)]
17. Hasnain, Z.; Fraser, A.K.; Georgess, D.; Choi, A.; Macklin, P.; Bader, J.S.; Peyton, S.R.; Ewald, A.J.; Newton, P.K. OrgDyn: Feature- and model-based characterization of spatial and temporal organoid dynamics. *Bioinformatics* **2020**, *36*, 3292–3294. [[CrossRef](#)]
18. Deininger, L.; Jung-Klawitter, S.; Mikut, R.; Richter, P.; Fischer, M.; Karimian-Jazi, K.; Breckwolddt, M.O.; Bendszus, M.; Heiland, S.; Kleesiek, J.; et al. An AI-based segmentation and analysis pipeline for high-field MR monitoring of cerebral organoids. *Sci. Rep.* **2023**, *13*, 21231. [[CrossRef](#)]
19. Albanese, A.; Swaney, J.M.; Yun, D.H.; Evans, N.B.; Antonucci, J.M.; Velasco, S.; Sohn, C.H.; Arlotta, P.; Gehrke, L.; Chung, K. Multiscale 3D phenotyping of human cerebral organoids. *Sci. Rep.* **2020**, *10*, 21487. [[CrossRef](#)]

20. Paşca, A.M.; Sloan, S.A.; Clarke, L.E.; Tian, Y.; Makinson, C.D.; Huber, N.; Kim, C.H.; Park, J.-Y.; O'Rourke, N.A.; Nguyen, K.D.; et al. Functional cortical neurons and astrocytes from human pluripotent stem cells in 3D culture. *Nat. Methods* **2015**, *12*, 671–678. [[CrossRef](#)]
21. Sloan, S.A.; Darmanis, S.; Huber, N.; Khan, T.A.; Birey, F.; Caneda, C.; Reimer, R.; Quake, S.R.; Barres, B.A.; Paşca, S.P. Human Astrocyte Maturation Captured in 3D Cerebral Cortical Spheroids Derived from Pluripotent Stem Cells. *Neuron* **2017**, *95*, 779–790.e6. [[CrossRef](#)]
22. Masselink, W.; Reumann, D.; Murawala, P.; Pasierbek, P.; Taniguchi, Y.; Bonnay, F.; Meixner, K.; Knoblich, J.A.; Tanaka, E.M. Broad applicability of a streamlined ethyl cinnamate-based clearing procedure. *Development* **2019**, *146*, dev166884. [[CrossRef](#)] [[PubMed](#)]
23. Qian, X.; Song, H.; Ming, G.-L. Brain organoids: Advances, applications and challenges. *Development* **2019**, *146*, dev166074. [[CrossRef](#)] [[PubMed](#)]
24. Berger, E.; Magliaro, C.; Paczia, N.; Monzel, A.S.; Antony, P.; Linster, C.L.; Bolognin, S.; Ahluwalia, A.; Schwamborn, J.C. Millifluidic culture improves human midbrain organoid vitality and differentiation. *Lab Chip* **2018**, *18*, 3172–3183. [[CrossRef](#)]
25. Qian, X.; Su, Y.; Adam, C.D.; Deutschmann, A.U.; Pather, S.R.; Goldberg, E.M.; Su, K.; Li, S.; Lu, L.; Jacob, F.; et al. Sliced human cortical organoids for modeling distinct cortical layer formation. *Cell Stem Cell* **2020**, *26*, 766–781.e9. [[CrossRef](#)]
26. Teng, Y.; Zhao, Z.; Tasnim, F.; Huang, X.; Yu, H. A scalable and sensitive steatosis chip with long-term perfusion of in situ differentiated HepaRG organoids. *Biomaterials* **2021**, *275*, 120904. [[CrossRef](#)] [[PubMed](#)]
27. Mansour, A.A.; Gonçalves, J.T.; Bloyd, C.W.; Li, H.; Fernandes, S.; Quang, D.; Johnston, S.; Parylak, S.L.; Jin, X.; Gage, F.H. An in vivo model of functional and vascularized human brain organoids. *Nat. Biotechnol.* **2018**, *36*, 432–441. [[CrossRef](#)]
28. Rambani, K.; Vukasinovic, J.; Glezer, A.; Potter, S.M. Culturing thick brain slices: An interstitial 3D microperfusion system for enhanced viability. *J. Neurosci. Methods* **2009**, *180*, 243–254. [[CrossRef](#)]
29. Garcez, P.P.; Loiola, E.C.; Madeiro da Costa, R.; Higa, L.M.; Trindade, P.; Delvecchio, R.; Nascimento, J.M.; Brindeiro, R.; Tanuri, A.; Rehen, S.K. Zika virus impairs growth in human neurospheres and brain organoids. *Science* **2016**, *352*, 816–818. [[CrossRef](#)]
30. Krenn, V.; Bosone, C.; Burkard, T.R.; Spanier, J.; Kalinke, U.; Calistri, A.; Salata, C.; Rilo Christoff, R.; Pestana Garcez, P.; Mirazimi, A.; et al. Organoid modeling of Zika and herpes simplex virus 1 infections reveals virus-specific responses leading to microcephaly. *Cell Stem Cell* **2021**, *28*, 1362–1379.e7. [[CrossRef](#)] [[PubMed](#)]
31. Matus, A.; Bernhardt, R.; Bodmer, R.; Alaimo, D. Microtubule-associated protein 2 and tubulin are differently distributed in the dendrites of developing neurons. *Neuroscience* **1986**, *17*, 371–389. [[CrossRef](#)] [[PubMed](#)]
32. Renner, H.; Grabos, M.; Becker, K.J.; Kagermeier, T.E.; Wu, J.; Otto, M.; Peischard, S.; Zeuschner, D.; TsyTsyura, Y.; Disse, P.; et al. A fully automated high-throughput workflow for 3D-based chemical screening in human midbrain organoids. *eLife* **2020**, *9*, e52904. [[CrossRef](#)] [[PubMed](#)]
33. Zhong, S.; Zhang, S.; Fan, X.; Wu, Q.; Yan, L.; Dong, J.; Zhang, H.; Li, L.; Sun, L.; Pan, N.; et al. A single-cell RNA-seq survey of the developmental landscape of the human prefrontal cortex. *Nature* **2018**, *555*, 524–528. [[CrossRef](#)]
34. Stachowiak, E.K.; Benson, C.A.; Narla, S.T.; Dimitri, A.; Chuye, L.E.B.; Dhiman, S.; Harikrishnan, K.; Elahi, S.; Freedman, D.; Brennand, K.J.; et al. Cerebral organoids reveal early cortical maldevelopment in schizophrenia-computational anatomy and genomics, role of FGFR1. *Transl. Psychiatry* **2017**, *7*, 6. [[CrossRef](#)]
35. Jorfi, M.; D'Avanzo, C.; Tanzi, R.E.; Kim, D.Y.; Irimia, D. Human neurospheroid arrays for in vitro studies of Alzheimer's disease. *Sci. Rep.* **2018**, *8*, 2450. [[CrossRef](#)] [[PubMed](#)]
36. Yakoub, A.M.; Sadek, M. Development and characterization of human cerebral organoids: An optimized protocol. *Cell Transplant.* **2018**, *27*, 393–406. [[CrossRef](#)]
37. Donato, R. S100: A multigenic family of calcium-modulated proteins of the EF-hand type with intracellular and extracellular functional roles. *Int. J. Biochem. Cell Biol.* **2001**, *33*, 637–668. [[CrossRef](#)]
38. Vives, V.; Alonso, G.; Solal, A.C.; Joubert, D.; Legraverend, C. Visualization of S100B-positive neurons and glia in the central nervous system of EGFP transgenic mice. *J. Comp. Neurol.* **2003**, *457*, 404–419. [[CrossRef](#)]
39. Bedner, P.; Dupper, A.; Hüttmann, K.; Müller, J.; Herde, M.K.; Dublin, P.; Deshpande, T.; Schramm, J.; Häussler, U.; Haas, C.A.; et al. Astrocyte uncoupling as a cause of human temporal lobe epilepsy. *Brain A J. Neurol.* **2015**, *138*, 1208–1222. [[CrossRef](#)]
40. Miranda-Negrón, Y.; García-Arrarás, J.E. Radial glia and radial glia-like cells: Their role in neurogenesis and regeneration. *Front. Neurosci.* **2022**, *16*, 1006037. [[CrossRef](#)]
41. Fujiyama, F.; Fritschy, J.M.; Stephenson, F.A.; Bolam, J.P. Synaptic localization of GABA(A) receptor subunits in the striatum of the rat. *J. Comp. Neurol.* **2000**, *416*, 158–172. [[CrossRef](#)]
42. Wang, P.; Eshaq, R.S.; Meshul, C.K.; Moore, C.; Hood, R.L.; Leidenheimer, N.J. Neuronal gamma-aminobutyric acid (GABA) type A receptors undergo cognate ligand chaperoning in the endoplasmic reticulum by endogenous GABA. *Front. Cell. Neurosci.* **2015**, *9*, 188. [[CrossRef](#)] [[PubMed](#)]
43. Felts, L.; Kohli, V.; Marr, J.; Schumacher, J.; Schlicker, O. An Introduction to Computational Clearing. 2020. Available online: <https://www.leica-microsystems.com/science-lab/life-science/an-introduction-to-computational-clearing/> (accessed on 25 October 2024).

44. Schneider, C.A.; Rasband, W.S.; Eliceiri, K.W. NIH Image to ImageJ: 25 years of image analysis. *Nat. Methods* **2012**, *9*, 671–675. [[CrossRef](#)]
45. Collins, J.A.; Schandi, C.A.; Young, K.K.; Vesely, J.; Willingham, M.C. Major DNA fragmentation is a late event in apoptosis. *J. Histochem. Cytochem.* **1997**, *45*, 923–934. [[CrossRef](#)] [[PubMed](#)]
46. Kroemer, G.; Galluzzi, L.; Vandenabeele, P.; Abrams, J.; Alnemri, E.S.; Baehrecke, E.H.; Blagosklonny, M.V.; El-Deiry, W.S.; Golstein, P.; Green, D.R.; et al. Classification of cell death: Recommendations of the Nomenclature Committee on Cell Death 2009. *Cell Death Differ.* **2009**, *16*, 3–11. [[CrossRef](#)] [[PubMed](#)]
47. Lancaster, M.A.; Renner, M.; Martin, C.-A.; Wenzel, D.; Bicknell, L.S.; Hurles, M.E.; Homfray, T.; Penninger, J.M.; Jackson, A.P.; Knoblich, J.A. Cerebral organoids model human brain development and microcephaly. *Nature* **2013**, *501*, 373–379. [[CrossRef](#)] [[PubMed](#)]
48. Otsu, N. A Threshold Selection Method from Gray-Level Histograms. *IEEE Trans. Syst. Man Cybern.* **1979**, *9*, 62–66. [[CrossRef](#)]
49. Cai, H.; Yang, Z.; Cao, X.; Xia, W.; Xu, X. A new iterative triclass thresholding technique in image segmentation. *IEEE Trans. Image Process.* **2014**, *23*, 1038–1046. [[CrossRef](#)] [[PubMed](#)]
50. Nickels, S.L.; Modamio, J.; Mendes-Pinheiro, B.; Monzel, A.S.; Betsou, F.; Schwamborn, J.C. Reproducible generation of human midbrain organoids for in vitro modeling of Parkinson’s disease. *Stem Cell Res.* **2020**, *46*, 101870. [[CrossRef](#)] [[PubMed](#)]
51. Smits, L.M.; Reinhardt, L.; Reinhardt, P.; Glatza, M.; Monzel, A.S.; Stanslowsky, N.; Rosato-Siri, M.D.; Zanon, A.; Antony, P.M.; Bellmann, J.; et al. Modeling Parkinson’s disease in midbrain-like organoids. *npj Park. Dis.* **2019**, *5*, 5. [[CrossRef](#)]
52. Bolognin, S.; Fossépré, M.; Qing, X.; Jarazo, J.; Ščančar, J.; Moreno, E.L.; Nickels, S.L.; Wasner, K.; Ouzren, N.; Walter, J.; et al. 3D Cultures of Parkinson’s Disease-Specific Dopaminergic Neurons for High Content Phenotyping and Drug Testing. *Adv. Sci.* **2019**, *6*, 1800927. [[CrossRef](#)]
53. Kerr, J.F.R.; Wyllie, A.H.; Currie, A.R. Apoptosis: A Basic Biological Phenomenon with Wideranging Implications in Tissue Kinetics. *Br. J. Cancer* **1972**, *26*, 239–257. [[CrossRef](#)] [[PubMed](#)]
54. Monzel, A.S.; Smits, L.M.; Hemmer, K.; Hachi, S.; Moreno, E.L.; van Wuellen, T.; Jarazo, J.; Walter, J.; Brüggemann, I.; Boussaad, I.; et al. Derivation of Human Midbrain-Specific Organoids from Neuroepithelial Stem Cells. *Stem Cell Rep.* **2017**, *8*, 1144–1154. [[CrossRef](#)] [[PubMed](#)]
55. Wilson, E.S.; Newell-Litwa, K. Stem cell models of human synapse development and degeneration. *Mol. Biol. Cell* **2018**, *29*, 2913–2921. [[CrossRef](#)] [[PubMed](#)]
56. Tanaka, Y.; Cakir, B.; Xiang, Y.; Sullivan, G.J.; Park, I.-H. Synthetic Analyses of Single-Cell Transcriptomes from Multiple Brain Organoids and Fetal Brain. *Cell Rep.* **2020**, *30*, 1682–1689.e3. [[CrossRef](#)] [[PubMed](#)]
57. Porciúncula, L.O.; Goto-Silva, L.; Ledur, P.F.; Rehen, S.K. The age of brain organoids: Tailoring cell identity and functionality for normal brain development and disease modeling. *Front. Neurosci.* **2021**, *15*, 674563. [[CrossRef](#)]
58. Dezonne, R.S.; Sartore, R.C.; Nascimento, J.M.; Saia-Cereda, V.M.; Romão, L.F.; Alves-Leon, S.V.; de Souza, J.M.; Martins-de-Souza, D.; Rehen, S.K.; Gomes, F.C.A. Derivation of Functional Human Astrocytes from Cerebral Organoids. *Sci. Rep.* **2017**, *7*, 45091. [[CrossRef](#)] [[PubMed](#)]
59. Wang, D.D.; Bordey, A. The astrocyte odyssey. *Prog. Neurobiol.* **2008**, *86*, 342–367. [[CrossRef](#)] [[PubMed](#)]
60. Mariani, J.; Coppola, G.; Zhang, P.; Abyzov, A.; Provini, L.; Tomasini, L.; Amenduni, M.; Szekeley, A.; Palejev, D.; Wilson, M.; et al. FOXG1-Dependent Dysregulation of GABA/Glutamate Neuron Differentiation in Autism Spectrum Disorders. *Cell* **2015**, *162*, 375–390. [[CrossRef](#)] [[PubMed](#)]
61. Zayat, V.; Kuczynska, Z.; Liput, M.; Metin, E.; Rzonca-Niewicz, S.; Smyk, M.; Mazurczak, T.; Goszczanska-Ciuchta, A.; Leszczynski, P.; Hoffman-Zacharska, D.; et al. The Generation of Human iPSC Lines from Three Individuals with Dravet Syndrome and Characterization of Neural Differentiation Markers in iPSC-Derived Ventral Forebrain Organoid Model. *Cells* **2023**, *12*, 339. [[CrossRef](#)]
62. Djuric, U.; Zadeh, G.; Aldape, K.; Diamandis, P. Precision histology: How deep learning is poised to revitalize histomorphology for personalized cancer care. *npj Precis. Oncol.* **2017**, *1*, 22. [[CrossRef](#)] [[PubMed](#)]
63. Coudray, N.; Ocampo, P.S.; Sakellaropoulos, T.; Narula, N.; Snuderl, M.; Fenyö, D.; Moreira, A.L.; Razavian, N.; Tsirigos, A. Classification and mutation prediction from non-small cell lung cancer histopathology images using deep learning. *Nat. Med.* **2018**, *24*, 1559–1567. [[CrossRef](#)] [[PubMed](#)]

**Disclaimer/Publisher’s Note:** The statements, opinions and data contained in all publications are solely those of the individual author(s) and contributor(s) and not of MDPI and/or the editor(s). MDPI and/or the editor(s) disclaim responsibility for any injury to people or property resulting from any ideas, methods, instructions or products referred to in the content.